

A minimal pathway for polarity establishment and centrosplindlin-independent cytokinesis based on AIR-1 inhibition of ECT-2

Ondrej Maxian and Michael Glotzer

April 26, 2024

Abstract

In early *Caenorhabditis elegans* embryos, contractility is partially controlled by the protein ECT-2, which acts through the GTPase RhoA to activate myosin and cortical flows. Centrosomal Aurora A (AIR-1) locally inhibits ECT-2, leading to larger-scale myosin flows that amplify ECT-2 asymmetries in both polarization and cytokinesis (Longhini and Glotzer, 2022). In this study, we construct a mathematical model to determine how dynamics of ECT-2 during polarization and cytokinesis are shaped by the AIR-1 cue and myosin flows.

1 Introduction

The anterior-posterior axis of the nematode *C. elegans* is determined in the zygote, shortly after the egg is fertilized. The position of sperm entry dictates the posterior pole. This event triggers myosin-dependent, anterior-directed cortical flows that facilitate the segregation of anterior and posterior PAR proteins into distinct domains (Munro et al., 2004; Lang and Munro, 2017; Gross et al., 2019).

Recent studies implicated Aurora A kinase, AIR-1, as a crucial factor required to initiate these cortical flows (Klinkert et al., 2019; Kapoor and Kotak, 2019; Longhini and Glotzer, 2022). AIR-1 associates with the sperm centrosome, which is the sperm-derived structure that promotes polarity establishment (Hannak et al., 2001). Recent work (Longhini and Glotzer, 2022) showed that AIR-1 impacts dynamics on the cortex by inhibiting the Rho GEF ECT-2. Specifically, ECT-2 dissociates from the posterior membrane in an AIR-1 dependent manner, and it contains a consensus site for AIR-1 that is required for AIR-1 responsiveness. During polarization, ECT-2 exhibits posterior depletion and anterior enrichment, a pattern of accumulation that requires cortical myosin flows.

However, unlike the anterior PAR proteins, which have residence times on the order of one hundred seconds (Robin et al., 2014), ECT-2 cannot be strongly advected, as it exchanges rapidly between the cytoplasm and the cortex on timescales of a few seconds, appearing to preferentially bind to the cortex at myosin-enriched sites (Longhini and Glotzer, 2022). Consequently, it remains unclear how a short residence time, preferential recruitment by myosin, and weak advection by cortical flows, could combine to generate the observed ECT-2 asymmetries during polarization.

A similar set of events occur upon anaphase onset, coincident with cytokinesis (Longhini and Glotzer, 2022). At first glance, cytokinesis and polarization appear quite different, as by the time cytokinesis is reached, the centrosomes have matured, accumulated much more AIR-1, and moved farther away from the cortex. Yet there remains a strong, ultra-sensitive dependence between the distance of the centrosome from the nearest cortical domain and the amount of cortical ECT-2 at that site; proximal centrosomes correlated with a reduction in cortical ECT-2. It is therefore possible that the same mechanisms that control polarity establishment reoccur in cytokinesis.

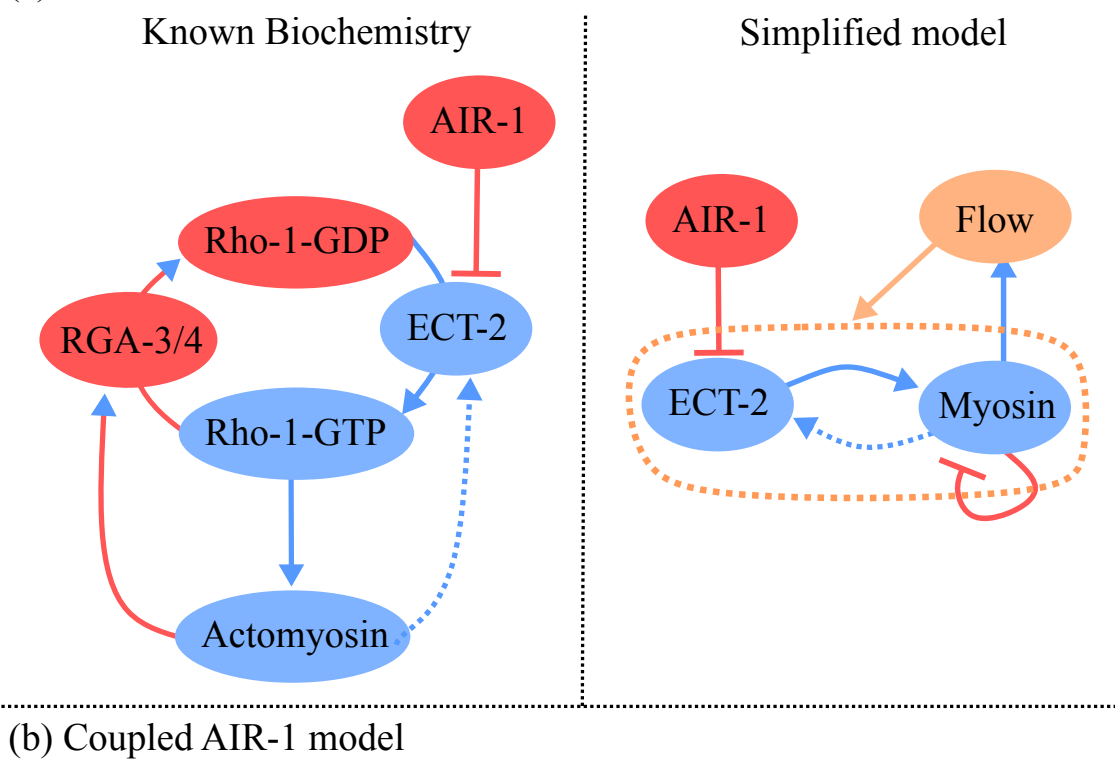
In this study, we set out to answer a basic question: what is the minimal set of interactions that can explain the dynamics of ECT-2 and myosin during both polarity establishment and central-spindlin cytokinesis? To do this, we construct a mathematical model that uses an AIR-1 signal from the centrosomes, which we assume is transported to the cortex by diffusion, as an input to a basic model of contractility of the type previously examined by others (Michaux et al., 2018; Michaud et al., 2022).

1.1 Basic model of contractility

The general schematic of our model (as well as how it corresponds to the known biochemistry) is shown in Fig. 1(a), and the mathematical details are presented in Appendix A.2. AIR-1 inhibits ECT-2, and ECT-2 activates myosin (through Rho). Myosin feeds back on ECT-2 through direct recruitment, and through advection by flows. Finally, there is delayed negative feedback of myosin accumulation (through RGA-3/4-dependent inactivation of RHO-1) (Michaux et al., 2018). To constrain unknown model parameters, we incorporate known experimental measurements for the turnover rates of each molecule and flow speeds, and further assume that

1. 10% of ECT-2 is bound to the cortex at steady state in wild-type embryos (our own unpublished(?) measurements).
2. 30% of myosin is bound to the cortex at steady state in wild-type embryos (Gross et al., 2019, Fig. S3j).

(a) Cortex model



(b) Coupled AIR-1 model

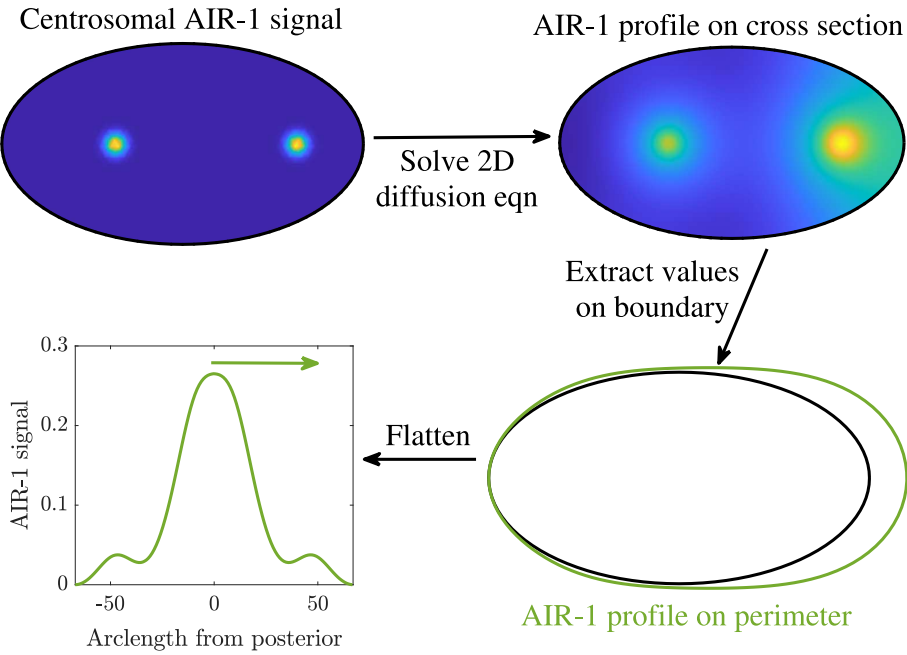


Figure 1: Modeling schematic for this study. (a) The model of the cortex, with the known biochemistry on the left and our simplified model on the right. This model takes the AIR-1 signal as input, and the equations are given in (S3). (b) Procedure for determining the AIR-1 signal. Given centrosome positions (shown are centrosomes in cytokinesis in wild-type embryos), we solve for the AIR-1 profile on the cross section using equation (S1), then formulate a one-dimensional AIR-1 profile by extracting the values on the boundary.

3. There is a modest increase (two-fold) in the recruitment rate of ECT-2 due to cortical myosin, in a myosin concentration-dependent manner.

In the Appendix, we use these assumptions to constrain the model parameters.

1.1.1 Theoretical analysis of the model

With the biochemical parameters constrained, the dynamics of flow and contractility can be understood in terms of two parameters: the hydrodynamic lengthscale, or the distance localized contractions could move components of the cortex (Mayer et al., 2010), and the flow speed for a given change in the myosin concentration. For the dynamics to be unstable, localized disturbances must be able to grow in time. Intuitively, this should occur when the flow speed is large and the hydrodynamic lengthscale is small, so that the disturbance is not spread out over a large region of the domain, but remains localized, and still generates large flows into/out of the peak.

In Fig. 2, we report the results of a stability analysis of our model (in the absence of the AIR-1 cue), which segregates the dynamics into three regimes based on the number of unstable modes in Fourier analysis (see Appendix). The stability diagram in Fig. 2(a) shows that the most unstable behavior occurs for high flow speeds and small lengthscales, as expected intuitively. Sampling parameters from each of the three regimes, and then tracking the response to a random disturbance reveals how the dynamics change in the three regimes (Fig. 2(b–d)). In the stable regime, all disturbances decay to the uniform steady state almost immediately, while in the intermediate regime, some of the modes are unstable, resulting in an overall pattern of contractility which slowly grows over time.

The most interesting regime in the cortex model is the excitable regime, where all modes are unstable (Fig. 2(d)). In this case, we see the formation of a steady state number of pulses, which are advected throughout the domain by the flows they generate. The spacing between the pulses is controlled by the hydrodynamic lengthscale; in Fig. 2(d), the lengthscale is 8% of the perimeter, or 16% of the half perimeter (which we call the embryo length). Thus, when two pulses become 32% embryo length ($2 \times$ the hydrodynamic lengthscale) apart, a “dead zone” emerges between the pulses that cannot “feel” either pulse. Instabilities there give rise to a new pulse. This process repeats, so that at “steady” state, the number of pulses is set by the spacing of $2 \times$ the hydrodynamic lengthscale (in Fig. 2(d), this translates to three pulses in half the embryo perimeter).

Understanding the regimes of the cortex model in which the embryo operates is vital to understanding the dynamics of polarization and central-spindlin-independent cytokinesis. While it is

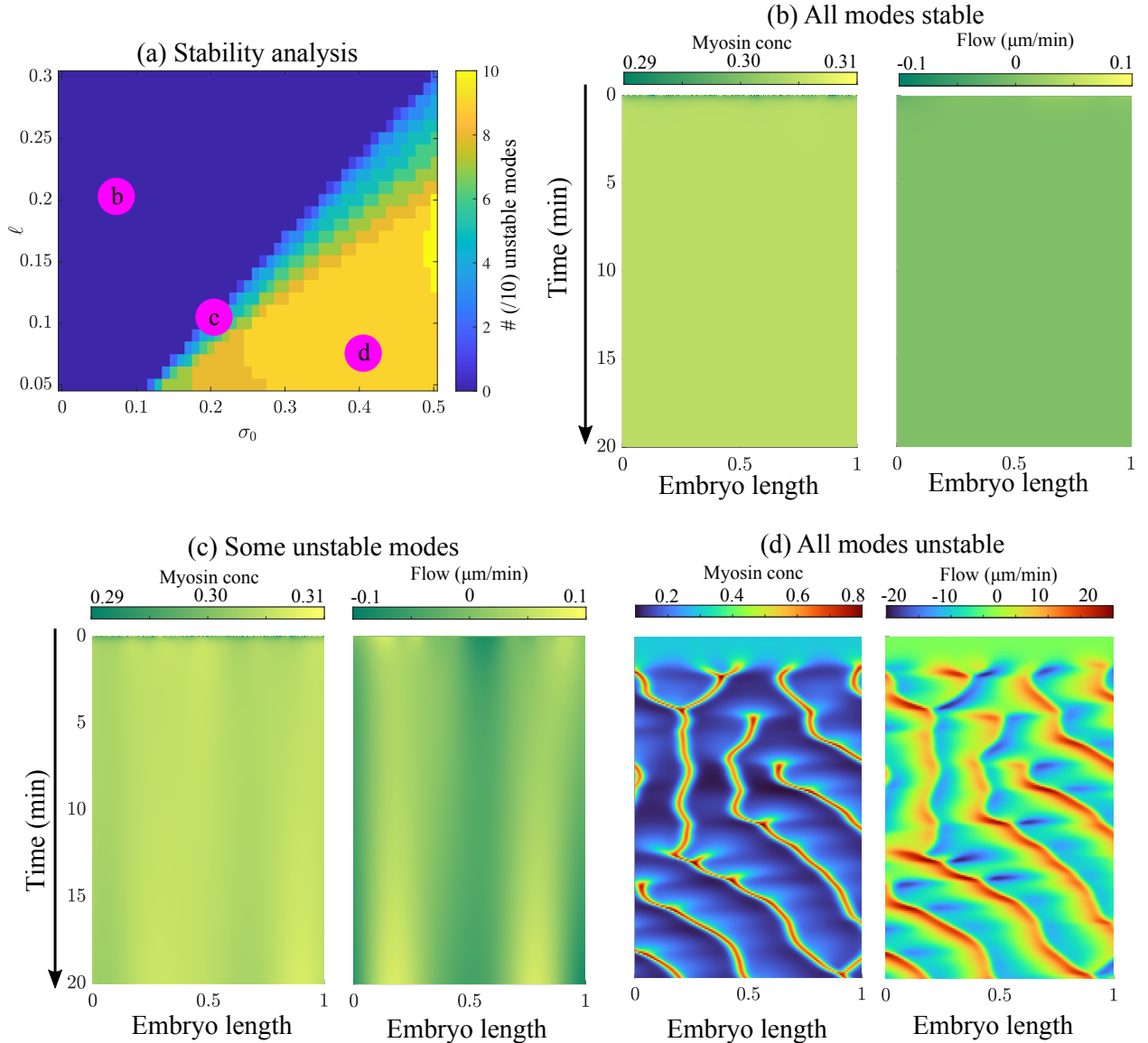


Figure 2: Linear stability analysis of the uniform state, and resulting types of model behavior. (a) Number (out of the first ten) of unstable modes in stability analysis (see Appendix), which is a proxy for how chaotic the system is. (b) When all modes are stable, perturbations decay back to the uniform state. (c) When some modes are unstable, perturbations in some wavelengths are amplified, while others decay. Our minimal model falls in this regime. (d) When all modes are unstable, there are pulsatile dynamics, with pulses forming, and then combining. The combination of pulses (or their transport) gives space for new pulses to form, and at steady state the number of pulses is set by the spacing of twice the hydrodynamic lengthscale.

known that Rho in establishment phase can generate pulses as in the excitable regime (Fig. 2(d)), these pulses are *not* essential for establishing polarity (Michaux et al., 2018, Fig. 7). Consequently, in our “minimal” model of polarity establishment, we operate in a regime where spontaneous pulses do not arise. We show that moving into the excitable regime presents a unique set of challenges; in particular, while cues can establish initial pulses in the right places, other pulses will still emerge spontaneously, even in places where inhibitory cues are still active.

1.2 Coupled model of AIR-1

As an input to the cortex model, we solve for the AIR-1 profile on the boundary of a two-dimensional cross section of the embryo. Figure 1(b) provides an overview of this process: for each embryo type, we obtain the centrosome positions, then solve a diffusion equation to obtain the AIR-1 profile on the entire embryo cross section. Evaluating the AIR-1 concentration (which has arbitrary units) on the boundary then gives a profile on the embryo perimeter, which we flatten out to a single periodic dimension. The mathematical details of this process are discussed in Appendix A.1; here it suffices to list the following assumptions that go into our model:

1. During cytokinesis, the centrosomes have radius about $2 \mu\text{m}$. The radius during polarization is 10% of this.
2. AIR-1 is activated on the centrosomes.
3. Active AIR-1 diffuses towards the cortex according to Fick’s law.
4. A global phosphatase activity inactivates AIR-1 throughout the cytoplasm.

Setting the level of global phosphatase activity is a non-trivial undertaking. As shown in Appendix A.1, low levels of phosphatase activity give high global AIR-1 levels, which translate to low ECT-2 levels everywhere. Such levels were shown to block pseudocleavage in central spindle-independent cytokinesis, due to low contractility (Afshar et al., 2010; Kotak et al., 2016). Our choice is to set the phosphatase activity so that centrosomes close to the posterior pole (in polarization) have a negligible AIR-1 concentration in the anterior (< 1% of the anterior concentration).

2 Results

2.1 The centrosome distance determines the strength of polarization

In cell polarization, both centrosomes sit very close to the posterior cortex (about $1 \mu\text{m}$ away (Cowan and Hyman, 2004)) and have size about $0.2 \mu\text{m}$ (compared to $2 \mu\text{m}$ in cytokinesis). They

also contain substantially less total AIR-1 than in cytokinesis; here we assume that the amount scales with the area, so that the amount of AIR-1 on each centrosome during polarization is 1% of that for cytokinesis. To explore the effect of centrosome distance and location, we position centrosomes at a distance 1, 5, and 10 μm from the posterior pole, and measure the resulting AIR-1 signal. There is a significant decrease in the AIR-1 signal as we move the centrosomes back from the cell boundary, with centrosomes 5 μm away giving a decrease of 50% in AIR-1, and 10 μm giving an almost nonexistent AIR-1 signal.

Given these AIR-1 signals, we run the model forward in time to reach a steady state for polarization. In the absence of PAR proteins, it is known that the AIR-1/ECT-2 signal from the centrosomes leads to transient clearing of myosin from the posterior pole, and that the myosin profile reverts back to a uniform state after the centrosomes move towards the cell equator (Gross et al., 2019, Fig. 2E). Figure 3(c) shows that our simulations reproduce the initial smaller-scale clearing of myosin and ECT-2. Under wild-type conditions, we predict an ECT-2 clearance (defined as the size of the region near the cue where $E < 0.095$) of about 20% perimeter, which translates to roughly 10 μm on either side of the pole, in good agreement with experimental observations in PAR mutants (Gross et al., 2019, Fig. 2E).¹ The flow speed of at most 5–6 $\mu\text{m}/\text{min}$ also matches observations in PAR mutants (Gross et al., 2019, Fig. 2G).

In the model, changing the distance between the centrosomes and the cortex affects the quantitative values of the asymmetries and the time to reach them, but it does not affect the myosin peak location, which is controlled by the hydrodynamic lengthscale and thus occurs around 60% embryo length regardless (40% embryo length from the posterior pole; Fig. 3(d)). Similar to previous observations (Bienkowska and Cowan, 2012, Fig. 3F), the time to reach a 10% myosin asymmetry (which we use as a proxy for symmetry breaking) increases from less than 25 seconds at a distance of 1 μm to about 50 seconds at a distance of 5 μm . However, our model predicts an exponential scaling of the time to symmetry breaking at very large distances; this does not match the linear trend up to 10 μm that was previously reported (Bienkowska and Cowan, 2012, Fig. 3F).

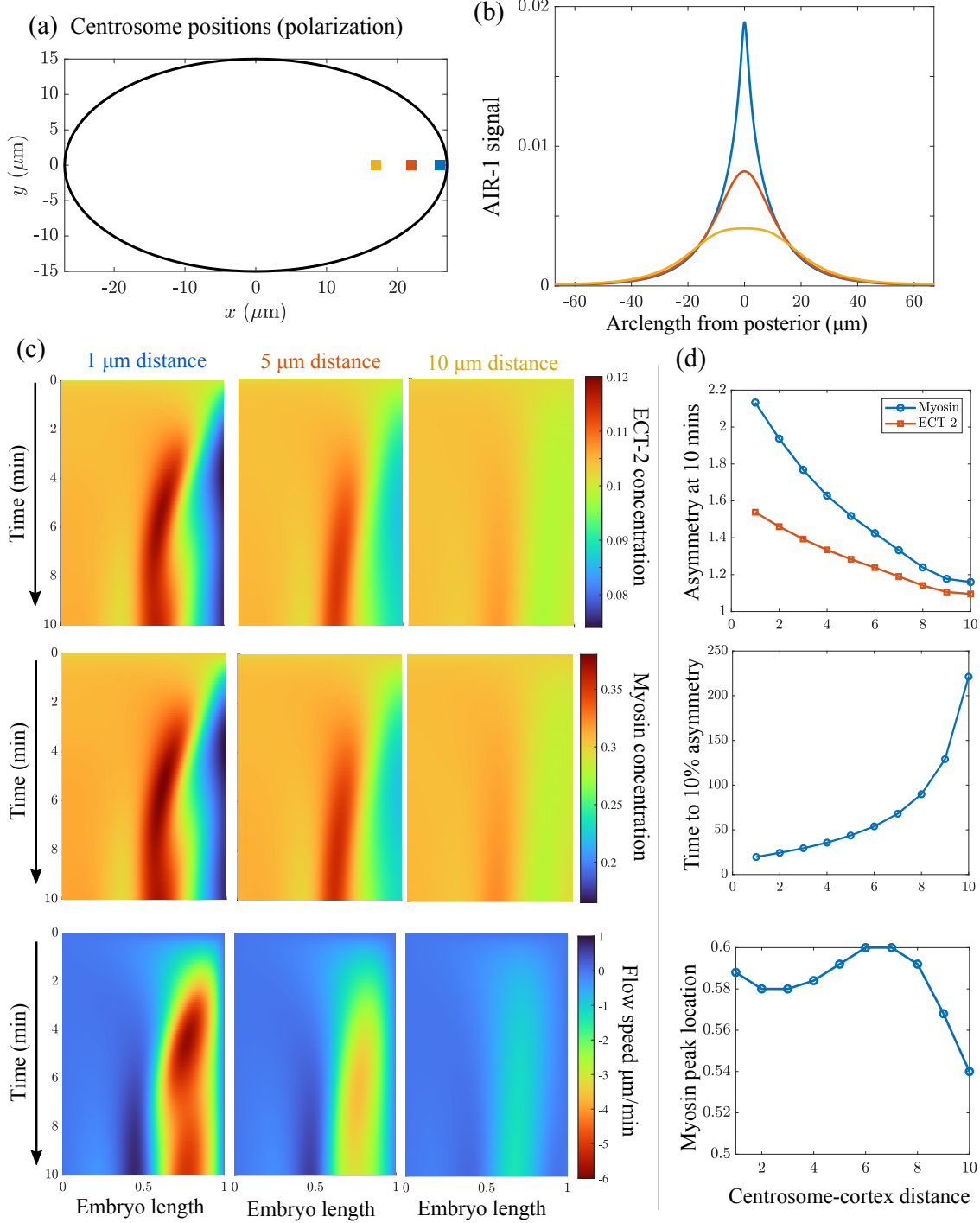


Figure 3: Centrosome locations set polarization dynamics. (a) The location of the centrosomes in our polarization simulations; we position both centrosomes 1, 5, and 10 μm away from the cell boundary. (b) The resulting AIR-1 signals along the cell perimeter. (c) The dynamics of polarization, starting from the uniform state, with the computed AIR-1 signal. We show the ECT-2 concentration (top), myosin concentration (middle), and flow speed (bottom) in a pseudo-kymograph, with time on the y axis, and the A/P axis on the x axis (A at left and P at right). (d) Summary statistics as a function of distance. We show the maximum asymmetry in myosin and ECT-2 after 10 mins (top), the time to each a 10% myosin asymmetry (middle), and the myosin peak location (bottom), as a function of the centrosome-cortex distance.

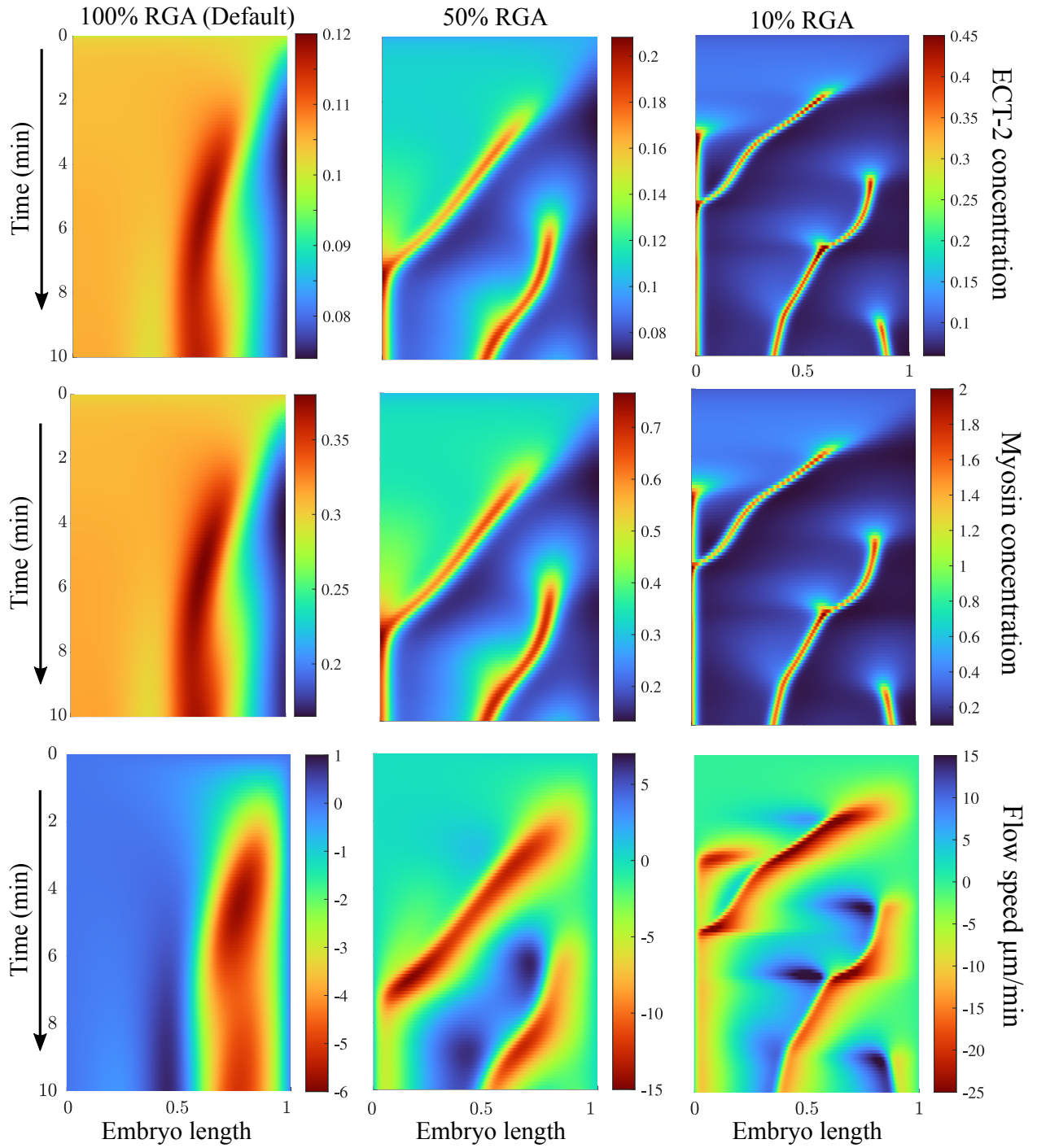


Figure 4: Dynamics of polarity establishment when RGA is depleted, in this case by reducing the nonlinear negative feedback for myosin to the indicated level. The left column shows the default parameters, while the middle column shows 50% negative feedback, and the right column shows 10% negative feedback. As in Fig. 3, rows show ECT-2 concentration, myosin concentration, and flow speed. In this case each has its own colorscale because of the high variability in the data between different parameter sets.

2.2 Effect of RGA Depletion

Previous work (Schonegg et al., 2007; Zanin et al., 2013; Michaux et al., 2018) has shown that depleting embryos of RGA leads to a hypercontractile anterior cap at the end of establishment phase. To test this in our model, we reduce the strength of myosin’s delayed negative feedback to 50% and 10% of the default parameter value, and examine the resulting dynamics in Fig. 4. Reducing the negative feedback levels has a strong qualitative effect, as the dynamics transition from the mostly stable (regime b in Fig. 2) to unstable and pulsatile. At 50% RGA depletion, the AIR-1 cue at the posterior pole generates a peak of ECT-2 and myosin which is advected towards the anterior pole in a flow of its own making. Once the peak moves far enough from the posterior pole, a second peak arises on the posterior. This peak makes its way towards the posterior pole as well. What results, then, is pulsatile contractility, but with a direction biased towards the anterior by the AIR-1 cue. Similar dynamics play out when negative feedback is reduced further to 10% of its original levels; in this case the peaks tend to be narrower, higher in concentration, and move faster.

While we successfully reproduce hypercontractility in embryos depleted of RGA, the model here predicts the formation of pulses, and then systematic transport of those pulses to the anterior over a timescale of minutes. This seems to be supported by experimental data (Michaux et al., 2018). However, experiments do not appear to show formation of new pulses in the posterior once the anterior domain is already set up. The discrepancy could be due to the PAR network (not accounted for in our model) inhibiting myosin on the posterior, which would suppress pulses there.

2.3 The relevance of rapid exchange

We have shown that long-range reorganization of ECT-2 is possible despite its short residence time. The driver of this reorganization is recruitment by myosin, which is longer-lived on the cortex than ECT-2. Yet, is there any benefit to having rapid turnover of ECT-2 on the cortex? To explore this question, in Fig. 5 we consider an alternative model where ECT-2 is advected, rather than recruited, by myosin. We accomplish this by making the ECT-2 lifetime an order of magnitude larger (without changing the percentage bound to the cortex), and removing the recruitment by myosin from the model. In this case, we observe dynamics that fall into the chaotic regime, with

¹The model “predicts” an A/P asymmetry of at most 1.5 during polarization, which matches experimental observations (Longhini and Glotzer, 2022, Fig. 1), but is calibrated to do so by changing the strength with which AIR-1 inhibits ECT-2.

pulses forming. Unlike in embryos depleted of RGA, where there are faster flow speeds (because myosin is inhibited), the increase in ECT-2 lifetime does not drive the pulse of ECT-2 all the way to the anterior pole, since flow speeds are not fast enough to transport it there. Rather, what happens is a peak which forms near the site of the AIR-1 signal, followed by a second peak which forms later in a more anterior location, where there is more space for an instability to grow.

2.4 Exploring other types of polarity cues

Previous reports on the contractility cue that drives polarization establishment identified two components of the cue: inhibition of contractility and removal of myosin (Gross et al., 2019). Our simulations using AIR-1 to inhibit ECT-2 have in principle captured the first cue; we therefore now ask about the second. In particular, we perform two simulations: one with the AIR-1 cue (centrosomes 1 μm from the posterior pole) active for five minutes, and a second with no AIR-1 cue and an initial unloading of myosin and ECT-2 at the posterior pole. The resulting dynamics over ten minutes are shown in Fig. 5. In both cases, transient cues or initial conditions ultimately relax to a steady state which is near uniform in ECT-2 and myosin with flow speeds which are near zero. Some small asymmetries remain as a result of operating our model near the unstable regime (see Fig. 2(c)).

For the transient AIR-1 cue, the flow starts at zero, and steadily increases over five minutes time to give a flow speed of 6 $\mu\text{m}/\text{min}$. Turning off the cue then brings the flow speeds below 2 $\mu\text{m}/\text{min}$ in three minutes time. By contrast, unloading myosin and ECT-2 from the posterior at $t = 0$ triggers a similar set of flows towards the anterior, but the flows are maximal at $t = 1$ minute, and then steadily decrease over time. Experimental data in PAR mutants show flows which are at a maximum almost immediately after polarity triggering, but the magnitude (5 $\mu\text{m}/\text{min}$) of these flows persist throughout polarity establishment phase (3–4 mins) (Gross et al., 2019, Fig. 2G). Thus, the true situation is likely a combination of local unloading and a persistent AIR-1 cue, similar to that reported in (Gross et al., 2019).

2.5 Dynamics of cytokinesis

In previous work (Longhini and Glotzer, 2022), we collected a series of data on how the ECT-2 accumulation on the posterior/anterior cortex during cytokinesis depends on the position of the corresponding centrosomes. In (Longhini and Glotzer, 2022, Fig. 7A), these are presented as individual embryos; here we average the individual embryos for each of the nine treatments and

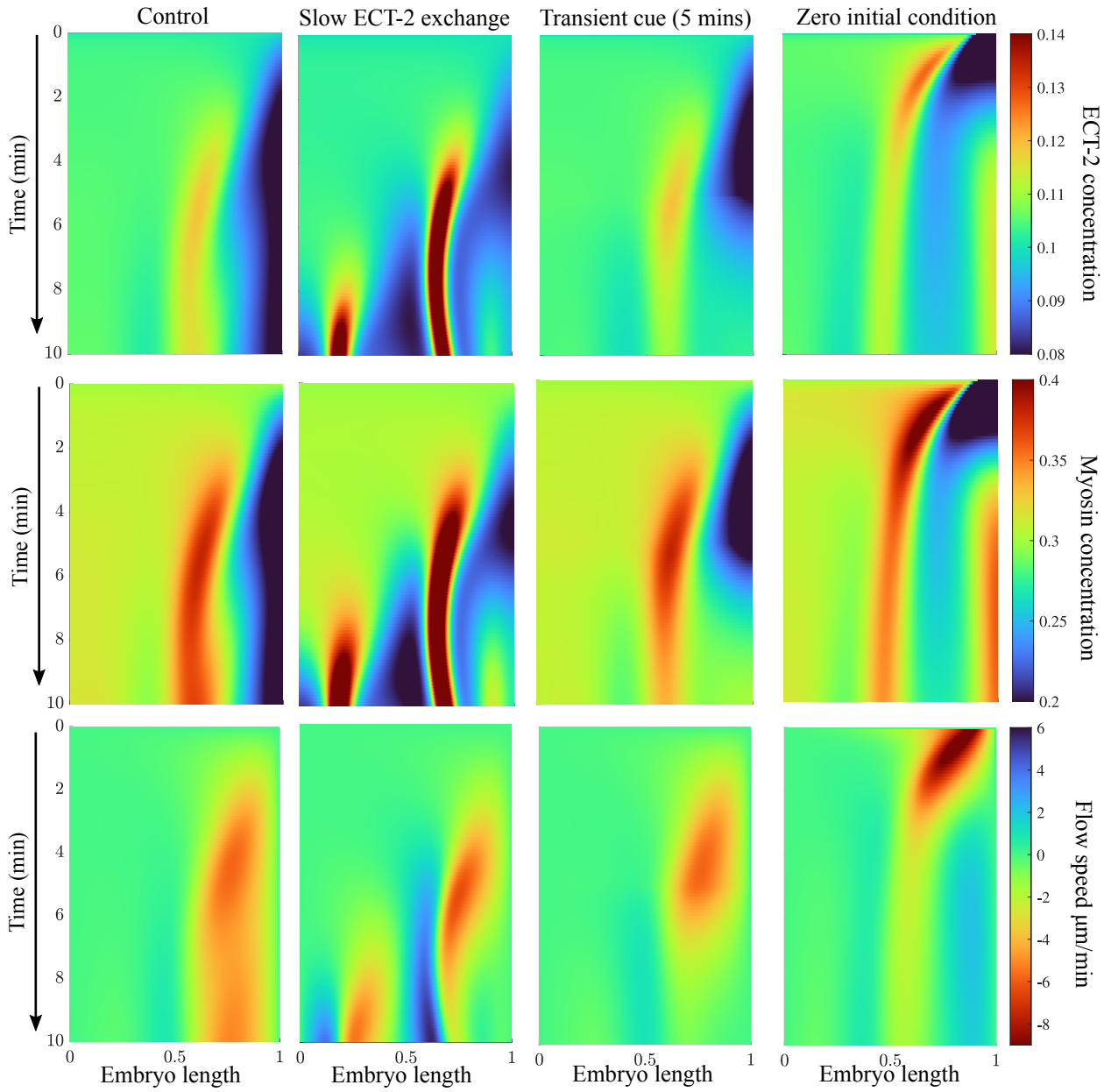


Figure 5: Adjusting conditions in polarization. Left panel: control parameters. Second from left: adjusting parameters so that, rather than be recruited by myosin, ECT-2 has a ten-fold longer residence time and is only advected. Third from left: Simulating the case where the AIR-1 cue (blue in Fig. 3) is applied for five minutes, after which we remove the AIR-1 signal and watch relaxation. Rightmost panel: Simulating the case of no AIR-1 signal, but an initial condition that has 10% of the domain at zero ECT-2 and myosin concentration.

show the mean values (error bars are a single standard error in the mean) in Fig. 6(c, right panel). We highlight two important aspects of this “S-shaped” curve: on both the anterior and posterior cortex, there is a plateau in the ECT-2 accumulation. That is, it appears that above or below a certain distance, the ECT-2 accumulation does not depend at all on the centrosome proximity. By contrast, for distances in the range $10\text{--}20 \mu\text{m}$, there is an ultra-sensitive dependence of the ECT-2 concentration on the proximity.

Using the centrosome positions measured in (Longhini and Glotzer, 2022), and repeated in Fig. 6(a), we first compute the AIR-1 signal (in arbitrary units) along the cell perimeter for each of the embryo treatments. We notice the high posterior levels of AIR-1 in *dhc-1* (RNAi) and *zyg-9;tpxl-1* embryos, which stand out from the rest. Despite the differences in AIR-1 signal in the posterior, these two embryo types have the same posterior ECT-2 signal as *zyg-9* embryos. In Appendix B, we use this observation to inform a simple saturation model for the effect of AIR-1 on ECT-2.

We use the AIR-1 signals from Fig. 6 as inputs to the same cortex model (Fig. 1(a)) that we parameterized under polarization conditions. Without changing any of the parameters, we simulate each embryo treatment to steady state, then record the ECT-2 concentration at the anterior/posterior pole at the time of the maximum asymmetry (approximately the steady state). Figure 6(b) shows the steady state distribution of ECT-2 and the steady state flow speeds for *dhc-1* (RNAi) and wild type embryos under cytokinesis conditions. The flows are of a realistic magnitude, and the ECT-2 concentration ratios between the anterior and posterior poles resemble the experimental measurements. Fig. 6(c) shows the ECT-2 accumulation on the anterior/posterior pole across all embryo treatments. We observe a plateau at the low end, corresponding to saturation of the AIR-1 signal, and a plateau at the high end, where myosin accumulation and flow is inhibited by RGA 3/4. In the middle, we see an ultra-sensitive dependence: moving from $10\text{--}20 \mu\text{m}$ centrosome distance gives a roughly two-fold change in ECT-2 accumulation, similar to the experimental data in Fig. 6(a). Thus our model, tuned for polarization, can also reproduce the dynamics of cytokinesis. This is a nontrivial undertaking; as shown in Appendix B, simpler models that do not amplify asymmetries by flow cannot reproduce the ultra-sensitive dependence for centrosome distances $10\text{--}20 \mu\text{m}$.

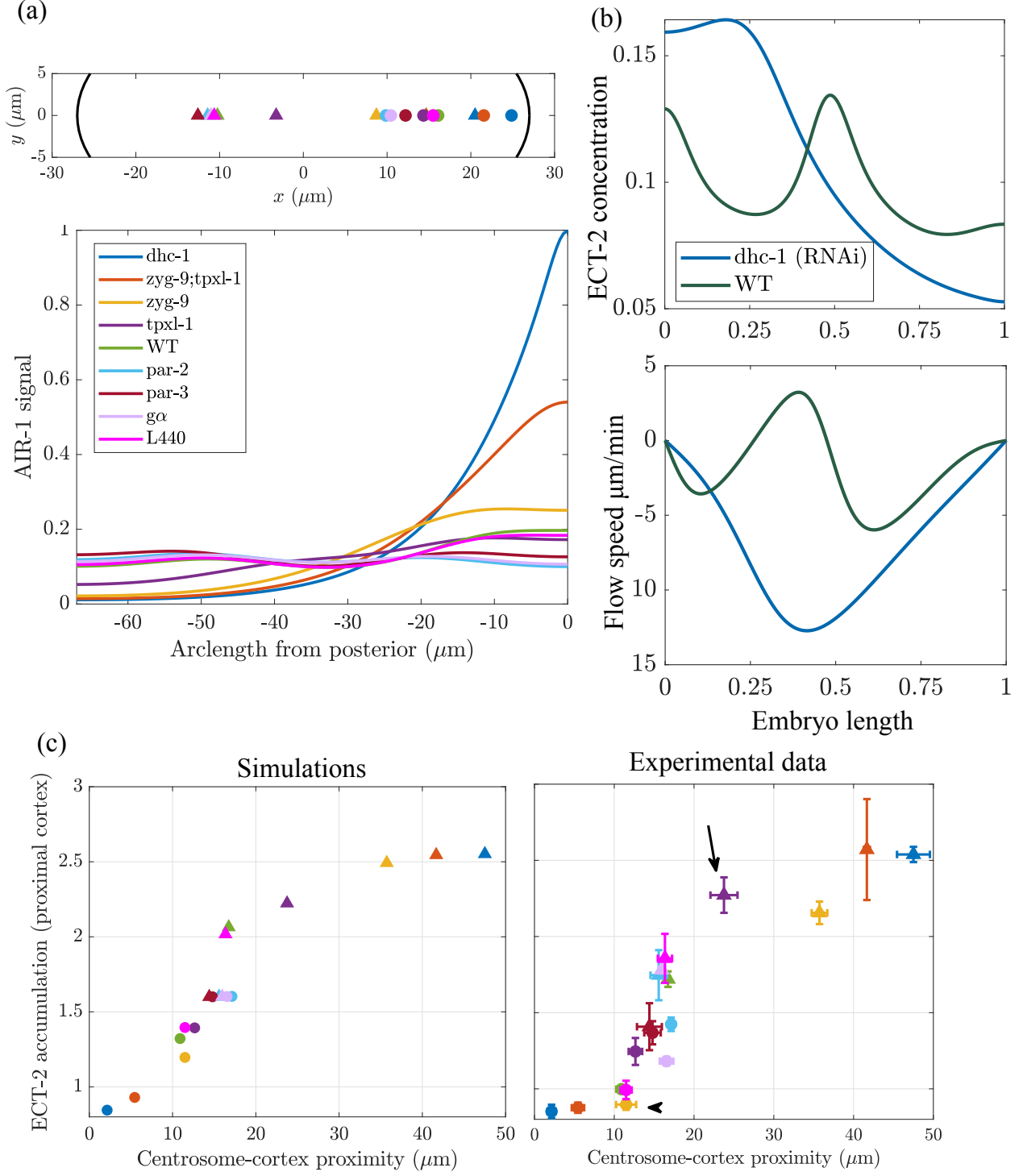


Figure 6: Extending the model to cytokinesis. (a) The centrosome positions for each embryo treatment, which are inputs to the diffusion model, and the corresponding AIR-1 signal on the cell perimeter, obtained from solving the diffusion equation (S1). (b) Steady states (profiles after ten minutes) in both *dhc-1* (blue) and wild type (green) embryos. (c) The simulation results and experimental data for how the ECT-2 accumulation on the proximal cortex depends on the centrosome positions (Longhini and Glotzer, 2022, Fig. 7A).

2.6 Comparing cytokinesis vs. polarization

3 Discussion

A Mathematical appendix

A.1 AIR-1 diffusion model

The contractility circuit is forced by a cue from the centrosomes which contain Aurora A (AIR-1), an inhibitor of ECT-2. We assume that the AIR-1 signal gets to the membrane by diffusion. Letting $a(\mathbf{x})$ be the concentration of AIR-1 in the two-dimensional embryo cross-section, we have the equation

$$\Delta a - \bar{k}^{\text{off}} a = -f \quad \mathbf{x} \in \Omega. \quad (\text{S1a})$$

$$\nabla a \cdot \mathbf{n} = 0 \quad \mathbf{x} \in \partial\Omega, \quad (\text{S1b})$$

where (S1a) is the diffusion equation for the concentration and (S1b) is a no-flux boundary condition through the boundary (here Ω represents the embryo area and $\partial\Omega$ represents the boundary). The signal $f(\mathbf{x})$ comes from the two centrosomes, which we model by Gaussian densities

$$f(\mathbf{x}) = \frac{C_0/D}{2\pi\sigma_c^2} \sum_{i=1}^2 \exp\left(\frac{-\|\mathbf{x} - \mathbf{x}_i\|^2}{2\sigma_c^2}\right). \quad (\text{S1c})$$

Here \mathbf{x}_i is the location of the i th centrosome (typically at some location $(x_i, 0)$), which changes depending on the embryo conditions. In addition to the centrosome location, the signal has two other parameters: C_0/D is the strength of the cue (the integral of $f(\mathbf{x})$ over the entire embryo cross-section, normalized by the cytoplasmic diffusion coefficient D), and σ_c is the centrosome “size” (the standard deviation of the Gaussian, which is roughly half the size of the centrosome). For cytokinesis, the centrosomes have size about $2 \mu\text{m}$, so we set $\sigma_c = 1 \mu\text{m}$. In polarization, the centrosomes have size about $0.2 \mu\text{m}$, so we set $\sigma_c = 0.1 \mu\text{m}$. The signal strength C_0/D is arbitrary; we set it to 1 for cytokinesis and 0.01 for polarization, thus assuming that the total amount of AIR-1 signal is proportional to centrosome area. The diffusion equation (S1a) also contains a basal rate of inactivation of AIR-1 (phosphatase activity). This introduces another parameter which is the inactivation rate relative to the diffusion coefficient in the cytoplasm (\bar{k}^{off} , units μm^{-2}).

We use a standard first-order finite element method to solve (S1a). In brief, the elliptical domain of the embryo is meshed into nodes and triangles (Persson and Strang, 2004), which define a set

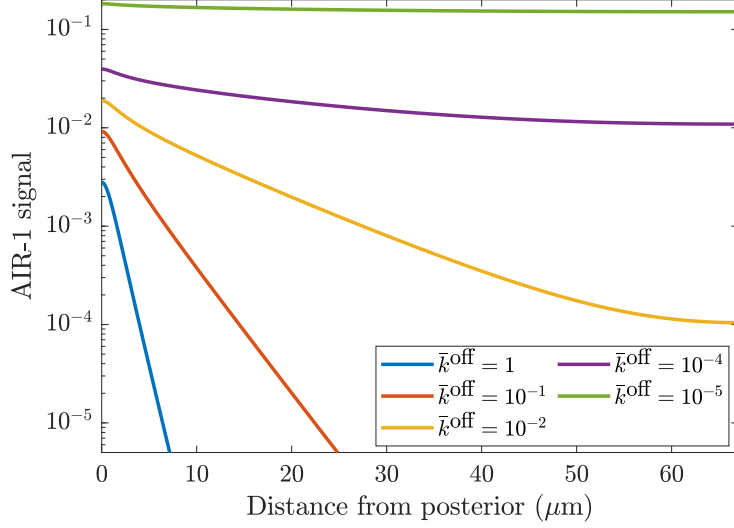


Figure S1: AIR-1 signal vs. distance from posterior under polarization conditions (blue squares in Fig. 3(a)). We vary the level of phosphatase activity \bar{k}^{off} until the posterior level is less than 1% of the anterior level, settling on $\bar{k}^{\text{off}} = 10^{-2} \mu\text{m}^{-2}$.

of linear Lagrangian basis functions ψ_k that are 1 at node \mathbf{x}_k and 0 everywhere else. Multiplying (S1a) by a basis function ψ_k , then integrating by parts using the boundary condition (S1b) gives

$$\sum_j \int_{\Omega} (\nabla \psi_k \cdot \nabla \psi_j) a_j d\mathbf{x} + \sum_j \int_{\Omega} \psi_k \psi_j a_j d\mathbf{x} = \sum_j \int_{\Omega} \psi_k \psi_j f_j d\mathbf{x}, \quad (\text{S2})$$

which can be written as the matrix equation $(\mathbf{K} + \bar{k}^{\text{off}} \mathbf{M}) \mathbf{a} = \mathbf{M} \mathbf{f}$, where \mathbf{M} is the so-called mass matrix and \mathbf{K} the stiffness matrix for finite elements. These matrices are assembled using standard techniques (Gockenbach, 2006, c. 7); see the github repository <https://github.com/omaxian/CElegansModel/> for code.

A.1.1 Constraining level of AIR-1 phosphatase activity

To constrain the level of phosphatase activity (parameter \bar{k}^{off}), we compute the profile of AIR-1 under polarization conditions (both centrosomes 1 μm from the posterior pole, with $C_0/D = 0.01$), and plot the resulting AIR-1 signal in Fig. S1. When the phosphatase activity is low, the no flux boundary condition traps AIR-1 inside the embryo, and the relative difference between posterior and anterior is small. Increasing the phosphatase activity disproportionately lowers AIR-1 levels on the anterior pole (since it is much farther from the centrosomes). We assume that anterior levels of AIR-1 during polarization are at most 1% of posterior levels; this constrains $\bar{k}^{\text{off}} = 10^{-2}$.

A.2 ECT-2/Myosin circuit

We here formulate the equations for the model shown in Fig. 1(a), where ECT-2 (through activating ρ) activates myosin at the cortex. To minimize the number of parameters, we consider a simplified version of the true dynamics (where ECT-2 signals myosin by activating rho) and formulate a model with two variables, E (for ECT-2) and M (for myosin). In dimensional units (denoted by hats), the equations we use are

$$\partial_t \hat{E} + \partial_{\hat{x}} (\hat{v} \hat{E}) = \hat{D}_E \partial_{\hat{x}}^2 E + k_E^{\text{on}} (1 + k_{ME} \hat{M}) \hat{E}_c - k_E^{\text{off}} \left(1 + k_{AE} \left(\frac{\hat{A}}{\hat{A}_c + \hat{A}} \right) \right) \hat{E} \quad (\text{S3a})$$

$$\partial_t \hat{M} + \partial_{\hat{x}} (\hat{v} \hat{M}) = \hat{D}_M \partial_{\hat{x}}^2 M + k_{EM} \hat{E}^2 \hat{M}_c - k_M^{\text{off}} \hat{M} - k_{fb} \hat{M}^4 \quad (\text{S3b})$$

$$\gamma \hat{v} = \eta \partial_{\hat{x}}^2 \hat{v} + \hat{\sigma}_0 \partial_{\hat{x}} \hat{M} \quad (\text{S3c})$$

$$\hat{E}_c = \frac{1}{hL} \left(E^{(\text{Tot})} L - \int_0^L \hat{E}(\hat{x}) d\hat{x} \right), \quad \hat{M}_c = \frac{1}{hL} \left(M^{(\text{Tot})} L - \int_0^L \hat{M}(\hat{x}) d\hat{x} \right). \quad (\text{S3d})$$

Each of the species ECT-2 and myosin evolves by

1. *Advection by cortical flows.* These are the terms $\partial_x(vE)$ and $\partial_x(vM)$.
2. *Diffusion in the cortex.* These are the terms $D_E \partial_x^2 E$, and $D_M \partial_x^2 M$.
3. *Binding to the cortex.* For ECT-2, there is a basal binding rate plus a linear enhancement by myosin. For myosin, the binding rate is proportional to the square of the ECT-2 concentration, without a basal binding rate. The motivation for this term is that myosin asymmetries are typically much stronger than ECT-2 asymmetries (Longhini and Glotzer, 2022; Munro et al., 2004; Mayer et al., 2010), and thus some nonlinearity is required. We choose the minimal such nonlinearity (see (Michaud et al., 2022, Eq. (1)) for another choice, where Rho is represented explicitly). The binding rate is also proportional to the cytoplasmic concentration of each protein, defined in (S3d), where L is the domain length, h is the cytoplasmic “thickness” (so that hL is the total area), and $A^{(\text{Tot})}$ is the concentration of protein A when all of it is bound to the cortex (Lang and Munro, 2022).
4. *Unbinding from the cortex.* For ECT-2, the unbinding rate is composed of a basal rate expressing the fast exchange of ECT-2, plus inhibition by AIR-1 according to (S7). Myosin unbinds with a basal rate (expressing the combination of inactivation and unbinding), which is enhanced by delayed negative feedback (the M^4 term). The form of this term is a coarse-grained version of previously-published work (Michaux et al., 2018). The model there considered rho (ρ) and RhoGAP (r) as the unknowns, with the production of RhoGAP proportional to ρ^3 and the inhibition of ρ proportional to $r\rho/(K + \rho)$. Here we coarse-grain this model into a

single term, with the inhibition proportional to M^4 .

Finally, the velocity equation (S4d) expresses the balance of active stress (which we assume is proportional to myosin concentration) with viscous stress and frictional resistance (Mayer et al., 2010).

A.2.1 Non dimensionalization

Because absolute concentrations are unknown, it is easiest to assign values to unknown parameters when they are in dimensionless form. To do this, we non-dimensionalize so that length is in units of the embryo perimeter L , time is in units of the bound myosin lifetime $1/k_M^{\text{off}}$, velocity is in units of $\sigma_0 / (\sqrt{\eta\gamma})$ (Bois et al., 2011) and concentration of species A is in units of $A^{(\text{Tot})}$. This gives new dimensionless variables

$$x = \hat{x}/L \quad t = \hat{t}k_M^{\text{off}} \quad M = \hat{M}/M^{(\text{Tot})} \quad E = \hat{E}/E^{(\text{Tot})} \quad v = \hat{v} / \left(\frac{\hat{\sigma}_0}{\sqrt{\eta\gamma}} \right), \quad (\text{S4a})$$

and a corresponding set of equations

$$\partial_t E + \sigma_0 \partial_x (vE) = D_E \partial_x^2 E + K_E^{\text{on}} (1 + K_{\text{ME}} M) E_c - K_E^{\text{off}} \left(1 + K_{\text{AE}} \left(\frac{A}{A_c + A} \right) \right) E \quad (\text{S4b})$$

$$\partial_t M + \sigma_0 \partial_x (vM) = D_M \partial_x^2 M + K_{\text{EM}} E^2 M_c - M - K_{\text{fb}} M^4 \quad (\text{S4c})$$

$$v = \ell^2 \partial_x^2 v + \ell \partial_x M \quad (\text{S4d})$$

$$E_c = 1 - \int_0^1 E(x) dx \quad M_c = 1 - \int_0^1 M(x) dx. \quad (\text{S4e})$$

The conversion from dimensional to dimensionless form is straightforward for most of these parameters. Since some (e.g. K_{AE} , K_{ME}) are unknown anyway, it is not useful to report how they relate to the dimensional parameters. There are some important parameters to highlight, however. In flow patterns, $\ell = (\sqrt{\eta/\gamma})/L$ is a hydrodynamic lengthsale (scaled by domain perimeter) expressing the connectivity of the cortex; local disturbances in myosin will typically propagate at most a distance ℓ . The parameter $\sigma_0 = \hat{\sigma}_0 / (L k_M^{\text{off}} \sqrt{\eta\gamma})$ expresses the strength of the flows; the dimensional velocity in $\mu\text{m}/\text{s}$ can be extracted by taking $v \times \sigma_0 L k_M^{\text{off}}$.

A.2.2 Numerical solution

We use standard numerical methods to solve (S4). We discretize the one-dimensional domain at N points with spacing $1/\Delta x$, and define the centered differentiation matrix \mathbf{D} and standard three points Laplacian differentiation matrix $\mathbf{\Delta}$. Given the myosin profile at time step n , we first

compute the velocity $v^{(n)}$ by solving $v^{(n)} = \ell^2 \Delta v^{(n)} + \ell \mathbf{D} M^{(n)}$. Once the velocity is computed the ECT-2 and myosin equations are solved by combining a first-order upwind finite volume scheme for the advection terms (Hundsdorfer et al., 2003, Sec. 1.4) with implicit treatment of the diffusion terms (using the standard three point Laplaian). The reaction terms are all treated explicitly, and time-stepping is first order accurate. Matlab code is available at the github repository <https://github.com/omaxian/CElegansModel1>.

A.2.3 Parameter estimation

Some of the parameters, as listed below, can be determined directly from experimental measurements,

1. The embryo cross section is an ellipse with approximate radii $27\text{ }\mu\text{m}$ and $15\text{ }\mu\text{m}$, which gives a perimeter $L = 134.6\text{ }\mu\text{m}$ (Goehring et al., 2011).
2. The variable ℓ is the hydrodynamic lengthscale. In dimensional units, this was measured to be approximately $13\text{ }\mu\text{m}$ (Mayer et al., 2010), which means $\ell = 0.1$ in (S4) (10% domain perimeter).
3. The myosin bound lifetime is about 15 s , so $k_M^{\text{off}} = 1/15\text{ s}^{-1}$.
4. We assume that all species have a dimensional diffusion coefficient $\hat{D}_{E/M} = 0.1\text{ }\mu\text{m}^2/\text{s}$ (Goehring et al., 2011; Gross et al., 2019; Robin et al., 2014). Rescaling length by L and time by k_M^{off} gives a dimensionless coefficient $D_E = D_M = 0.1/(L^2 k_M^{\text{off}}) = 4.6 \times 10^{-5}$.
5. The ECT-2 lifetime was measured using FRAP to be on the order of a few seconds (Longhini and Glotzer, 2022, Fig. 3D). In cytokinesis, we set $k_E^{\text{off}} = 0.33/\text{s}$, for a three second lifetime. Rescaling gives $K_E^{\text{off}} = k_E^{\text{off}}/k_M^{\text{off}} = 5$. The data show slightly faster recovery during polarization, so we increase k_E^{off} by 20% for those simulations.
6. For the negative feedback of myosin, we use the parameters determined in (Michaux et al., 2018). The feedback strength is obtained by assuming an equilibrium of RhoGAP in those equations (neglecting the basal binding rate which gives (in their notation)

$$K_{\text{fb}} = k_{\text{GAP}} \left(k_r^{\text{ass}} / k_r^{\text{diss}} \right) = 0.1(0.245/0.047) = 0.52/\text{s}$$

. Rescaling by k_M^{off} gives $K_{\text{fb}} = 7.8$ in our model.

These assumptions give values for all parameters except for K_E^{on} , K_{ME} , K_{AE} , A_c , K_{EM} , and σ_0 . Four of these parameters can be fit by considering the desired model behavior in the absence of AIR-1. Experimental data (Longhini and Glotzer, 2022, Fig. 1) show that the A/P ECT-2 ratio

is about 1.5:1, and that 10% of ECT-2 is bound to the cortex. A similar set of data (Gross et al., 2019, Figs. S2,S3) show that the A/P myosin ratio is about 2:1, with 30% of myosin is bound to the cortex, and cortical flows on the order $10 \mu\text{m}/\text{min}$.

Figure S2 shows how we incorporate these data to fix the simulation parameters. First, as shown at left, we fix the ECT-2 profile according to experimental observations, then adjust $K_{\text{EM}} = 50$ and $\sigma_0 = 0.2$, so that at steady state we obtain the myosin profile and flow speeds observed in experiments. Then, we recompute the steady state without inhibition by RGA, which results in a hypercontractile phenotype with more myosin in the anterior and larger flow speeds (dotted lines in bottom left plot), thus validating that our model gives qualitatively correct behavior. Similarly, in the right panel, we fix the myosin profile to correspond to experimental measurements, then adjust the parameters K_E^{on} and K_{ME} until we obtain the correct ECT-2 profile (top right plots). In particular, in each case we set K_E^{on} so that 10% of ECT-2 is bound to the cortex. Setting $K_{\text{ME}} = 0$ (with $K_E^{\text{on}} = 0.66$) gives no recruitment of ECT-2 by myosin, and the ECT-2 profile is only shaped by advection, and is consequently barely asymmetric. Increasing to $K_{\text{ME}} = 10/9$ (with $K_E^{\text{on}} = 0.5$) gives about 25% of ECT-2 recruited by myosin and a larger asymmetry. We settle on $K_{\text{ME}} = 10/3$ (with $K_E^{\text{on}} = 0.34$), which gives 50% of ECT-2 recruited by myosin, and the 1.5:1 A/P ratio we seek. This completes the selection of all parameters, except for K_{AE} and A_c .

To select $K_{\text{AE}} = 0.6$, we enforce that the max/min ECT-2 concentration is 1.5 under normal polarization conditions (left panel of Fig. 3). The threshold A_c does not come in during polarization because AIR-1 signals are low; as such we set its value according to the investigation in Section B.

A.2.4 Parameter adjustments: polarization

In Fig. 5, we modify the parameters to examine an alternative hypothesis where ECT-2 has a longer lifetime. We consider in particular $k_E^{\text{off}} = 1/25 \text{ s}^{-1}$ (25 s residence time instead of 2.5) and $K_E^{\text{on}} = 0.068$ to give a 10% bound ECT-2, and $K_{\text{ME}} = 0$, so that myosin doesn't recruit ECT-2. All other parameters take their default values (in particular, $\sigma = 0.2$).

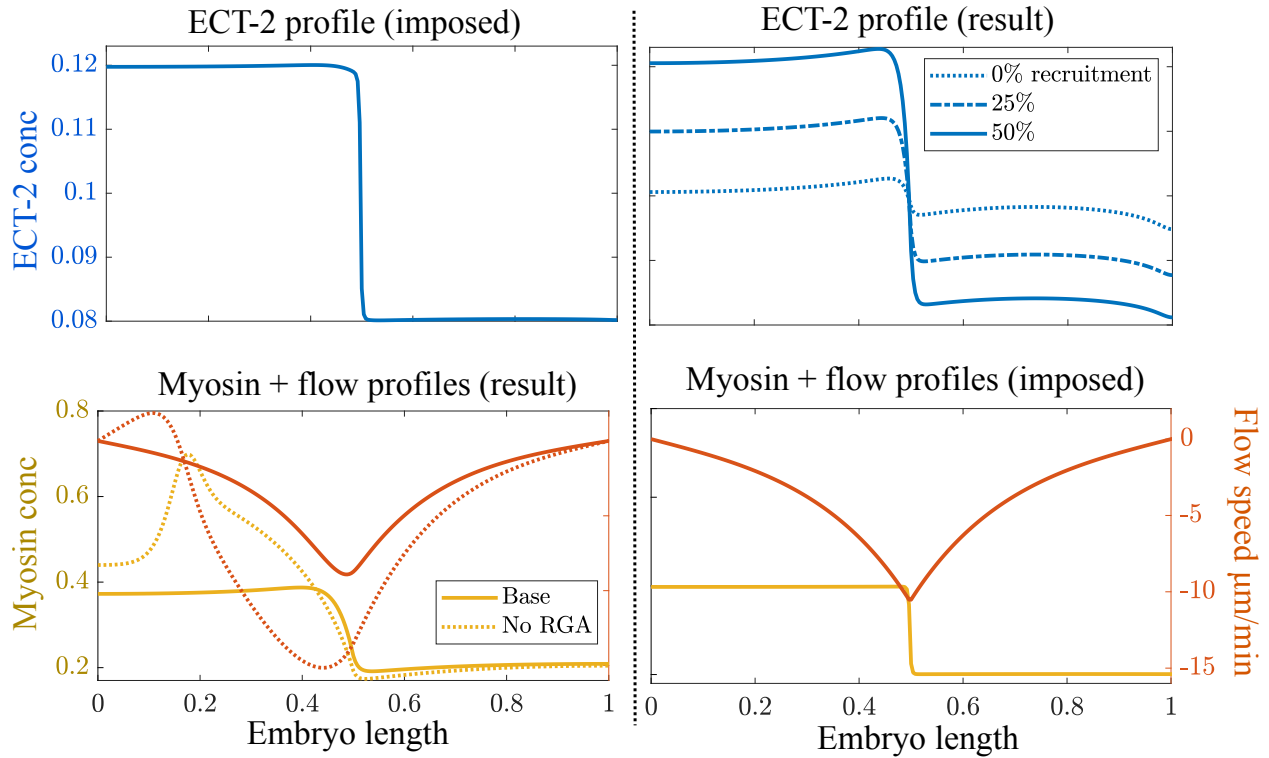


Figure S2: Validating our simple model of the cell cortex and setting the parameters. Left panels: we impose an ECT-2 profile that is 50% higher on the posterior than anterior, then measure the myosin and flow profiles with our chosen parameters. Right: we impose the myosin and corresponding flow profile, and examine the ECT-2 profiles with different rates of myosin recruitment.

A.2.5 Linear stability analysis of model equations

B Myosin-independent models for the ECT-2 response are inadequate

In the simplest possible model of ECT-2 dynamics, there is a local equilibrium of the binding rate and unbinding rate, where the latter increases in the presence of AIR-1,

$$k_E^{\text{on}} = k_E^{\text{off}} (1 + K_{\text{AE}} A) E, \quad (\text{S5})$$

and K_{AE} expresses the strength of inhibition. This steady state model predicts that the ECT-2 concentration relates to the AIR-1 concentration at the cortex via

$$E = \frac{k_E^{\text{on}} / k_E^{\text{off}}}{1 + K_{\text{AE}} A}, \quad (\text{S6})$$

which is a relationship with two unknown constants. Fitting these two unknown constants to the observed ECT-2 levels in *dhc-1* (RNAi) embryos (where the AIR-1 signal is approximately 1 at the posterior and 0 at the anterior) gives $k_E^{\text{on}} / k_E^{\text{off}} = 2.55$ and $K_{\text{AE}} = 2$. Substituting the AIR-1 levels from the other embryo treatments then gives the observed centrosome/ECT-2 accumulation plot shown in Fig. S3(a). There we see that the relationship (S6) correctly predicts saturation at low levels of AIR-1 (high centrosome-cortex distances), but fails to predict saturation at high AIR-1 levels (low distances) or ultra-sensitivity in between.

The AIR-1 signals we obtained in Fig. 6(a) show that the AIR-1 signal at the posterior doubles when we switch from *zyg-9;tpxl-1* (red) embryos to *dhc-1* embryos (blue). Yet, the experimental data in Fig. 6(a) show that the ECT-2 accumulation is unchanged. This tells us that there must be saturation in the AIR-1 inhibition dynamics; beyond some level, the amount of AIR-1 no longer impacts the inhibition strength. Based on the location of the plateau in the experimental data, it seems that this threshold level occurs around the posterior AIR-1 level in *zyg-9* embryos, which our data in Fig. 6(d) tells us is 0.2. Thus, we propose a new model where the local equilibrium is governed by

$$k_E^{\text{on}} = k_E^{\text{off}} \left(1 + K_{\text{AE}} \left(\frac{A}{A_c + A} \right) \right) E, \quad (\text{S7})$$

where $A_c = 0.2$. Once again fitting $k_E^{\text{on}} / k_E^{\text{off}} = 2.8$ and $K_{\text{AE}} = 2.8$ to the data for *dhc-1* embryos, we obtain the centrsome/ECT-2 plot shown in Fig. S3(b). There we see that we have correctly reduced the posterior ECT-2 levels in embryos with high AIR-1 signals to approach a plateau. However,

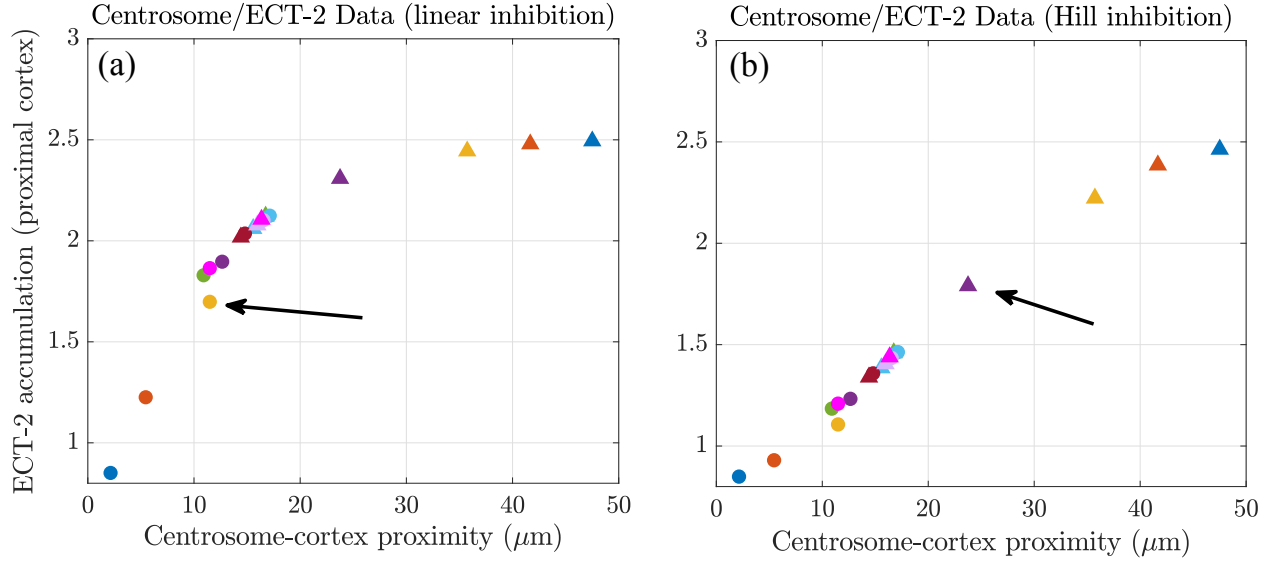


Figure S3: Simple models based on AIR-1/ECT-2 inhibition fail to capture the experimental data on accumulation vs. centrosome position. We consider (a) a linear inhibition model (S6), and (b) a linear model with saturation (S7) (Hill function). Compared to the data in Fig. 6, neither of these simple models capture the general S-shape of the curve, with plateaus at the low and high ends.

we also reduce the ECT-2 levels in the other embryos (especially *tpxl-1*; purple), and we still no longer see the ultra-sensitivity in distances 10–20 μm . We propose that the failure of these simple models comes from a lack of propagation of the AIR-1/ECT-2 signal via flows. As shown in Fig. 6(c), flows can exaggerate the smaller asymmetries, giving ultra sensitivity in the interior of the curve.

References

- Katayoun Afshar, Michael E Werner, Yu Chung Tse, Michael Glotzer, and Pierre Gönczy. Regulation of cortical contractility and spindle positioning by the protein phosphatase 6 *pph-6* in one-cell stage *c. elegans* embryos. *Development*, 137(2):237–247, 2010.
- Dominika Bienkowska and Carrie R Cowan. Centrosomes can initiate a polarity axis from any position within one-cell *c. elegans* embryos. *Current biology*, 22(7):583–589, 2012.
- Justin S Bois, Frank Jülicher, and Stephan W Grill. Pattern formation in active fluids. *Biophysical Journal*, 100(3):445a, 2011.

Carrie R Cowan and Anthony A Hyman. Centrosomes direct cell polarity independently of microtubule assembly in *c. elegans* embryos. *Nature*, 431(7004):92–96, 2004.

Mark S Gockenbach. *Understanding and implementing the finite element method*. SIAM, 2006.

Nathan W Goehring, Philipp Khuc Trong, Justin S Bois, Debanjan Chowdhury, Ernesto M Nicola, Anthony A Hyman, and Stephan W Grill. Polarization of par proteins by advective triggering of a pattern-forming system. *Science*, 334(6059):1137–1141, 2011.

Peter Gross, K Vijay Kumar, Nathan W Goehring, Justin S Bois, Carsten Hoege, Frank Jülicher, and Stephan W Grill. Guiding self-organized pattern formation in cell polarity establishment. *Nature physics*, 15(3):293–300, 2019.

Eva Hannak, Matthew Kirkham, Anthony A Hyman, and Karen Oegema. Aurora-a kinase is required for centrosome maturation in *caenorhabditis elegans*. *The Journal of cell biology*, 155(7):1109–1116, 2001.

Willem H Hundsdorfer, Jan G Verwer, and WH Hundsdorfer. *Numerical solution of time-dependent advection-diffusion-reaction equations*, volume 33. Springer, 2003.

Sukriti Kapoor and Sachin Kotak. Centrosome aurora a regulates rhogef ect-2 localisation and ensures a single par-2 polarity axis in *c. elegans* embryos. *Development*, 146(22):dev174565, 2019.

Kerstin Klinkert, Nicolas Levernier, Peter Gross, Christian Gentili, Lukas von Tobel, Marie Pierron, Coralie Busso, Sarah Herrman, Stephan W Grill, Karsten Kruse, et al. Aurora a depletion reveals centrosome-independent polarization mechanism in *caenorhabditis elegans*. *Elife*, 8:e44552, 2019.

Sachin Kotak, Katayon Afshar, Coralie Busso, and Pierre Gönczy. Aurora a kinase regulates proper spindle positioning in *c. elegans* and in human cells. *Journal of cell science*, 129(15):3015–3025, 2016.

Charles F Lang and Edwin Munro. The par proteins: from molecular circuits to dynamic self-stabilizing cell polarity. *Development*, 144(19):3405–3416, 2017.

Charles F Lang and Edwin M Munro. Oligomerization of peripheral membrane proteins provides tunable control of cell surface polarity. *Biophysical Journal*, 121(23):4543–4559, 2022.

Katrina M Longhini and Michael Glotzer. Aurora a and cortical flows promote polarization and cytokinesis by inducing asymmetric ect-2 accumulation. *Elife*, 11:e83992, 2022.

Mirjam Mayer, Martin Depken, Justin S Bois, Frank Jülicher, and Stephan W Grill. Anisotropies in cortical tension reveal the physical basis of polarizing cortical flows. *Nature*, 467(7315):617–621, 2010.

Ani Michaud, Marcin Leda, Zachary T Swider, Songeun Kim, Jiaye He, Jennifer Landino, Jenna R Valley, Jan Huisken, Andrew B Goryachev, George von Dassow, et al. A versatile cortical pattern-forming circuit based on rho, f-actin, ect2, and rga-3/4. *Journal of Cell Biology*, 221(8):e202203017, 2022.

Jonathan B Michaux, François B Robin, William M McFadden, and Edwin M Munro. Excitable rhoa dynamics drive pulsed contractions in the early *c. elegans* embryo. *Journal of Cell Biology*, 217(12):4230–4252, 2018.

Edwin Munro, Jeremy Nance, and James R Priess. Cortical flows powered by asymmetrical contraction transport par proteins to establish and maintain anterior-posterior polarity in the early *c. elegans* embryo. *Developmental cell*, 7(3):413–424, 2004.

Per-Olof Persson and Gilbert Strang. A simple mesh generator in matlab. *SIAM review*, 46(2):329–345, 2004.

François B Robin, William M McFadden, Baixue Yao, and Edwin M Munro. Single-molecule analysis of cell surface dynamics in *caenorhabditis elegans* embryos. *Nature methods*, 11(6):677–682, 2014.

Stephanie Schonegg, Alexandru T Constantinescu, Carsten Hoege, and Anthony A Hyman. The rho gtpase-activating proteins rga-3 and rga-4 are required to set the initial size of par domains in *caenorhabditis elegans* one-cell embryos. *Proceedings of the National Academy of Sciences*, 104(38):14976–14981, 2007.

Esther Zanin, Arshad Desai, Ina Poser, Yusuke Toyoda, Cordula Andree, Claudia Moebius, Marc Bickle, Barbara Conradt, Alisa Piekny, and Karen Oegema. A conserved rhogap limits m phase contractility and coordinates with microtubule asters to confine rhoa during cytokinesis. *Developmental Cell*, 26(5):496–510, 2013.